

Enhanced Photovoltaic Properties Induced by Ferroelectric Domain Structures in Organometallic Halide Perovskites

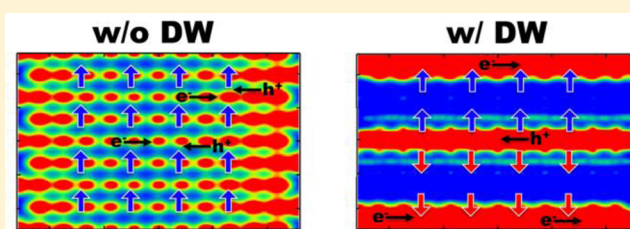
Fuzhen Bi,^{†,‡} Stanislav Markov,[§] Rulin Wang,[‡] YanHo Kwok,[§] Weijun Zhou,[§] Limin Liu,[‡] Xiao Zheng,[†] GuanHua Chen,[§] and ChiYung Yam^{*,‡,§}

[†]Hefei National Laboratory for Physical Sciences at the Microscale and Department of Chemical Physics, University of Science and Technology of China, Hefei, Anhui 230026, China

[‡]Beijing Computational Science Research Center, Beijing 100193, China

[§]Department of Chemistry, The University of Hong Kong, Pokfulam Road, Hong Kong, China

ABSTRACT: Organometallic halide perovskites have drawn substantial interest due to their outstanding performance in solar energy conversion and optoelectronic applications. The presence of ferroelectric domain walls in these materials has shown to have a profound effect on their electronic structure. Here, we use a density-functional-based tight-binding model, coupled to nonequilibrium Green's function method, to investigate the effects of ferroelectric domain walls on electronic transport properties and charge carrier recombination in methylammonium lead–iodide perovskite, MAPbI₃. With the presence of ferroelectric domain walls, segregation of transport channels for electrons and holes is observed, and the conductance of perovskites is substantially increased due to the reduced band gap. In addition, by taking into account interactions with photons in the vacuum environment, it is found that electron–hole recombination in perovskites with ferroelectric domain walls is drastically suppressed due to the segregation of carrier transport paths, which could enhance photovoltaic performance.



INTRODUCTION

Recently, organometallic halide perovskites have emerged as a new class of photovoltaic materials, and the field of perovskite-based photovoltaic devices has captured great attention within the energy harvesting community. Tremendous progress has been made in terms of device performance. Since the first use of organometallic halide perovskites in dye-sensitized solar cell by Kojima et al. in 2009,¹ the power conversion efficiencies (PCE) have shown an unprecedented increase from 3.8% to 20.1% over the past few years.^{2–4} This is the first time for a new photovoltaic technology with performance comparable to that of traditional commercial technology within such a short period. The primary advantage of these perovskites is that they can be solution-processed without the need of high-temperature treatment, making them an excellent material for low-cost and large-area optoelectronic applications. In addition, there are several outstanding optoelectronic properties of these materials, including possession of a tunable direct band gap in the visible to infrared regions as a function of composition,^{5,6} long electron and hole diffusion lengths together with high carrier mobilities, which suppress the recombination of photoexcited charge carriers,^{7–9} and strong optical absorption properties that allow solar cells of submicrometer thickness for sufficient light harvesting, which make perovskite-based solar cells a promising photovoltaic device.

Despite the rapid progress in perovskite-based photovoltaics, there are still problems in stability and environmental compatibility of these devices that hinder their widespread

deployment in the market. Before these devices can be tailored for greater efficiencies, many fundamental questions of the material that are key to their performance must be fully understood. A number of unusual characteristics have been reported for perovskite-based solar cells, such as current–voltage hysteresis,¹⁰ a giant dielectric constant,¹¹ switchable photovoltaic effect,¹² and reversible photoinduced material transformation.^{13,14} Among the fundamental properties, ferroelectricity^{15–18} has attracted much interest as it affects the charge-transfer mechanism and may have an important role for the enhancement of photovoltaic devices efficiency. Although the existence of ferroelectric domains in perovskite materials at room temperature is debated, domain engineering has been applied to establish and manipulate ferroelectric behavior in inorganic perovskites, and enhanced ferroelectric properties have been observed.^{19,20} In fact, the presence of switchable ferroelectric domains in MAPbI₃ perovskites has been demonstrated via piezoresponse force microscopy, with a domain size of about 100 nm. Most recently, Rakita et al. demonstrated the ferroelectric nature of MAPbI₃ by multiple experimental techniques and clarified the reason why ferroelectricity in MAPbI₃ seemed elusive. Contrary to previous studies, they used the dissipative part of permittivity and observed a remarkably clear ferroelectric hysteresis loop in

Received: March 31, 2017

Revised: April 28, 2017

Published: May 3, 2017

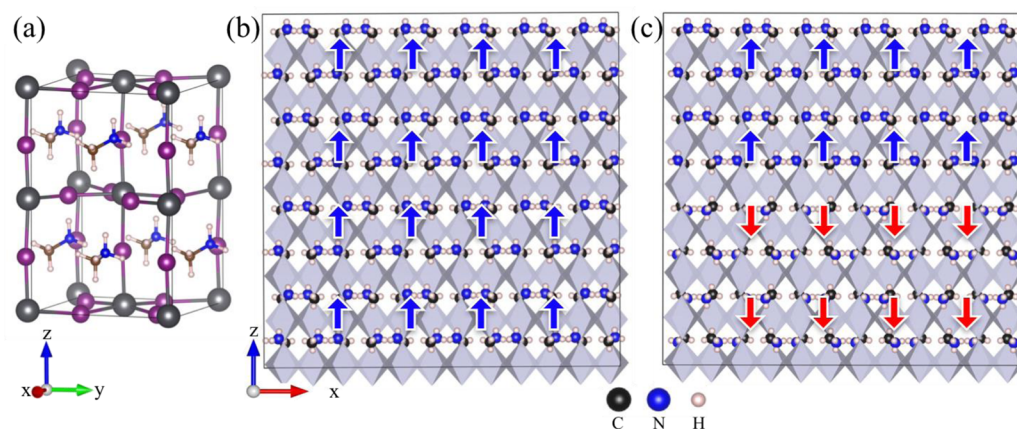


Figure 1. (a) Optimized tetragonal unit cell of MAPbI₃ perovskite. Device structures of a $6 \times 1 \times 4$ supercell with (b) single domain; and (c) domain structure that contains a tail-to-tail domain wall at the middle and head-to-head domain walls at upper and lower boundaries. Red arrows correspond to the polarization directions due to methylammonium cations.

tetragonal MAPbI₃ crystals.²¹ Moreover, theoretical studies show that organometallic halide perovskites exhibit spontaneous electric polarization, and its magnitude is found to be affected by the orientation of methylammonium cations.^{22–24} In addition, structures with ferroelectric alignment of methylammonium cations are shown to be more stable,^{25,26} and *ab initio* molecular dynamics demonstrated that MA cations can undergo collective motion and result in non-vanishing polarization.²⁷ It has been suggested that the electrostatic potential at ferroelectric domain walls can promote separation of photoexcited carriers and allow above-band gap open-circuit voltages.^{28,29} This makes it possible for PCE of perovskite-based photovoltaic devices to go beyond the Shockley–Queisser limit in conventional solar cells.³⁰ In addition, due to the structural flexibility of MAPbI₃, local domain structures may form under thermal conditions. It has been predicted that the resulting local electric fields may give rise to Rashba effect with a subpicosecond time scale.³¹ Recently, Monte Carlo combined with drift-diffusion simulations demonstrate reduced carrier recombination losses with the presence of nanodomains.³² Other first-principles simulations also reveal the effects of ferroelectric domain walls based on the electronic structure of closed systems and demonstrate their importance on photovoltaic applications of organometallic halide perovskites.^{33–36} However, the role of ferroelectric domain walls in electron transport and charge carrier recombination in organometallic halide perovskites remains unknown. To provide further insight into the properties of organometallic halide perovskites in relation to photovoltaic applications, we computationally study the impact of ferroelectricity on transport properties of MAPbI₃ perovskites based on nonequilibrium Green's function (NEGF) theory.³⁷ MAPbI₃ perovskite materials are parametrized for the DFTB method, and commendable agreement is achieved in comparison to extremely costly SOC-GW calculations.³⁸ This allows us to model device structures with tens of nanometer thickness, explicitly simulating their nonequilibrium properties under external bias. In particular, by incorporating electron–photon interactions in the NEGF formalism, we compare the rate of charge recombination of perovskites in different ferroelectric states. A substantial reduction of charge recombination rate of perovskites is found in the presence of ferroelectric domain structures. This result elucidates the contributions of ferroelectric domains to the outstanding

performance of organometallic halide perovskites for photovoltaic applications, and is useful not only for understanding, but also for engineering the performance of the energy conversion mechanism.

■ COMPUTATIONAL DETAILS

1. Atomic Models. The tetragonal phase of archetypal MAPbI₃ perovskite is chosen in our simulations as it is the stable phase at room temperature. The atomic structure of a 48-atom unit cell of MAPbI₃ is first relaxed with density-functional theory (DFT) using VASP package,³⁹ as shown in Figure 1a. The generalized gradient approximation (GGA) with Perdew–Burke–Ernzerhof (PBE) exchange–correlation functional⁴⁰ was adopted to calculate exchange and correlation energy. Nonlocal effects are described with the *vdw*-DF functional⁴¹ to take into account the weak interactions between organic cations and the inorganic cage. Core electrons are represented by projector augmented-wave (PAW) pseudopotentials.⁴² An energy cutoff of 400 eV and a $4 \times 4 \times 4$ Monkhorst–Pack *k*-point mesh are applied. Further increase of energy cutoff and *k*-points shows no significant difference. The initial relaxed atomic structure is obtained by conjugate gradient relaxation until the maximum atomic force is less than 0.01 eV/Å. To construct systems with ferroelectric domain walls, a supercell consisting of four tetragonal unit cells is stacked along the *z*-direction, where the orientations of methylammonium cations in the lower half of the supercell are rotated. This results in domain structure with a tail-to-tail charged domain wall formed at the middle of the supercell and head-to-head charged domain walls at two ends of the supercell. On the other hand, supercell of single domain is constructed with all organic cations aligned in the same direction. The dimensions of supercells are fixed to values of the optimized lattice constants of unit cell. The atomic structure of the supercell is then fully relaxed using $4 \times 4 \times 4$ Monkhorst–Pack *k*-point meshes with the same method mentioned above. For the study of transport properties, we construct homogeneous device structures on the basis of the optimized supercells. Devices with six supercells are aligned along the *x*-direction, which is the electronic transport direction. Each device contains a central region with channel length of 5.24 nm and is in contact with left and right electrodes. Thus, device structures of a $6 \times 1 \times 4$ supercell with 1152 atoms are constructed, and periodic boundary conditions

are applied to y - and z -directions of the devices. We present in Figure 1 the optimized unit cell and device structures.

2. DFTB Parametrization. We choose a self-consistent DFTB Hamiltonian for the transport modeling due to its favorable computational efficiency, as compared to DFT.⁴³ DFTB derives as an approximation of DFT, and its parametrization concerns both electronic structure and the so-called repulsive potentials, critical for atomic structure relaxation. However, we perform the structural relaxation of the models within DFT; therefore, for this study we deal only with electronic structure. Without going into the full details of self-consistent DFTB,⁴³ it is important to emphasize that the parameters in this case are per chemical element, and are very few. Specifically, the matrix elements of the Hamiltonian and overlap matrixes $h_{\mu\nu}^0$ and $s_{\mu\nu}$ are obtained by the two-center approximation, starting with a linear combination of atomic orbitals $\{\phi_\mu^A\}$:

$$h_{\mu\nu}^0 = \begin{cases} \varepsilon_\mu^A, & \text{for } \mu = \nu \in A \\ \langle \phi_\mu^A | \hat{T} + V_{\text{eff}}^A + V_{\text{eff}}^B | \phi_\nu^B \rangle, & \text{for } A \neq B \\ 0, & \text{otherwise} \end{cases} \quad (1)$$

$$s_{\mu\nu} = \langle \phi_\mu | \phi_\nu \rangle \quad (2)$$

Here, \hat{T} is the kinetic energy operator, and V_{eff}^A is the self-consistent effective potential. The above equations are solved in advance within all-electron DFT for all monatomic and diatomic pairs of chemical elements in a system. The accuracy of DFTB is dramatically improved if $\{\phi_\mu^A\}$ are compressed, as compared to their free atom counterpart, which is done by solving the Kohn–Sham equations for the atoms with an additional confining potential $(\mathbf{r}/r_0)^m$:

$$[\hat{T} + V_{\text{eff}}^A[n_A(\mathbf{r})] + (\mathbf{r}/r_0)^m] \phi_\mu = \varepsilon_\mu^A \phi_\mu(\mathbf{r}) \quad (3)$$

except for $h_{\mu\mu}^0$ where $r_0 = \infty$ is effectively used.

The confining potential holds the parameters of DFTB, r_0 and m . Because these parameters must be optimized per chemical element, for the problem at hand we need parameters for {Pb, I, C, N, H}. To reduce the effort, we start with the parametrization of {H, C, N, I} reported in ref 44 and extend the set to include Pb. We use density superposition as in ref 44, which allows for two distinct compression radii per element, that is, instead of the potential superposition in eq 1, as follows. First, the atomic density $n_A(\mathbf{r}_A)$ of each atom is found by a self-consistent calculation of eq 3 with $r_0 = r_d$. Next, $V_{\text{eff}}[n_A(\mathbf{r}_A) + n_B(\mathbf{r}_B)]$ is solved to replace $V_{\text{eff}}^A + V_{\text{eff}}^B$ in eq 1. However, the corresponding orbitals are not used in eq 1. Instead, eq 3 is solved again with a different compression radius, $r_0 = r_w$, from which a new set of orbitals is found and used in eqs 1 and 2.

In optimizing r_d , r_w , and m , we aimed to obtain the experimental band gap and band curvature at the conduction and valence band extrema, which are underlying the desirable optoelectronic properties of MAPbI₃ photocells. We used 6s²6p² minimal valence basis for Pb in DFTB. The addition of 5d or 6d orbitals yields noninteracting states far from the conduction/valence band edges, and is avoided; it did not improve the accuracy of DFTB but significantly raises the computational cost due to more than doubling the number of Pb orbitals. The atomic calculations corresponding to eq 3 are done at the all-electron DFT level, with PBE functional and scalar relativistic potential, due to the large atomic mass of Pb.

The atomic onsite energies (in hartrees) obtained for the free Pb atom are $\varepsilon_{6s} = -0.434869$ and $\varepsilon_{6p} = -0.129357$. The Hubbard parameters, on which the self-consistent term of DFTB pivots,⁴³ resulted in 0.210459 and 0.279609 hartree for the 6p and 6s orbitals correspondingly. These numbers agree very well with the free atom energies reported in the general DFTB parametrization for the periodic table.⁴⁵ Unfortunately, the published parametrization does not reproduce well the band structure of MAPbI₃, and we further optimized $r_d = 26.01$ Å and $r_w = 4.69$ Å for Pb, while setting $m = 4$, without the inclusion of spin–orbit coupling (SOC). However, it has been shown that the inclusion of SOC significantly alters the conduction band dispersion, reducing the bandgap, and that in the presence of SOC, the GW correction is necessary to yield the experimental value of the gap. In addition, it has been proposed that the Rashba effect driven by SOC can suppress carrier recombination due to a spin-forbidden transition.^{31,46} In view of that, we included SOC in the band-structure calculations with DFTB as implemented in DFTB+ computer code,⁴⁷ and reoptimized the compression radii of Pb for that case too: $r_d = 25.42$ Å and $r_w = 8.16$ Å, using published spin–orbit coupling constants for Pb (0.95 eV⁴⁸), I (0.66 eV⁴⁸), and C (0.009 eV⁴⁹), and ignoring spin–orbit effects in N and H.

In both cases, the optimization process considered the atomic and electronic structure of MAPbI₃ in the tetragonal phase (TET-p), as reported in ref 50, aiming to reproduce the experimental band gap of 1.6 eV. Figure 2 shows the band

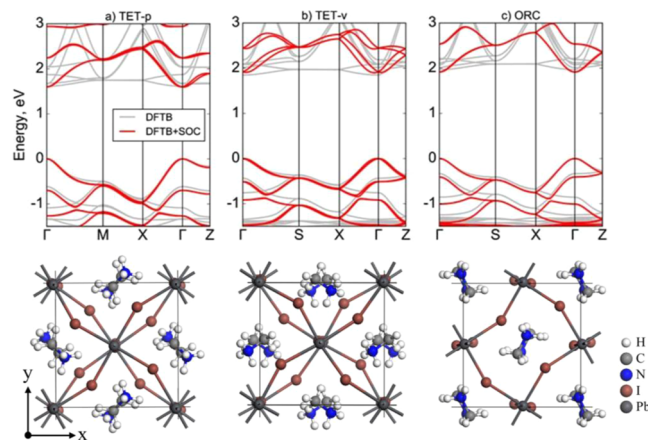


Figure 2. Band structures (upper panel) and the corresponding structures (bottom panel) of MAPbI₃ in tetragonal (a) TET-p and (b) TET-v, and orthorhombic (c) ORC structures calculated within DFTB without SOC (gray lines) and with SOC (red lines). The top of the valence band is taken as common energy reference. The results without SOC reproduce the features of the conduction and valence bands reported from scalar relativistic DFT report excluding relativistic and quasiparticle corrections.⁵⁰ The results with SOC improve the dispersion in the conduction band and agree very well with fully relativistic treatment with quasiparticle corrections.³⁸ In both cases, the band gap dependence on atomic structure as reported in ref 38 is accurately reproduced.

structures of all three unit cells of ref 50: two in the tetragonal phase, labeled TET-p (methylammonium cations oriented with parallel C–N bond) and TET-v (vertically oriented methylammonium cations), and one in the orthorhombic phase, labeled ORC. Both calculations, without SOC (gray lines) and with SOC (red lines), are shown for comparison. In Table 1 we compare the reported band gaps and average effective masses

Table 1. Comparison between the Band Gap and Effective Masses Obtained from DFTB without SOC/(with SOC) in This Work and with DFT⁵⁰ and SOC-GW³⁸ Calculation

	band gap [eV]				effective masses [m_0]		
	DFTB (+SOC)	PBE ⁵⁰	SOC-GW ³⁸		DFTB Γ -X/ Γ -Z	PBE ⁵⁰	SOC-GW ³⁸ Γ -X/ Γ -Z
TET-p	1.61 (1.60)	1.60	1.67	m_h	0.18/0.31 (0.19/0.29)	0.28	0.2/0.4
				m_e	2.9/0.1 (0.23/0.19)		
TET-v	1.85 (1.90)	1.82		m_h	0.29/0.31 (0.28/0.19)	0.30	
				m_e	3.4/0.1 (0.25/0.17)		
ORC	1.96 (1.95)	1.90		m_h	0.25/0.27 (0.26/0.27)	0.39	
				m_e	2.3/0.1 (0.23/0.22)		

obtained with DFTB (again without and with SOC) against those reported in ref 50, DFT, scalar relativistic potential, and ref 38, fully relativistic SOC-GW calculations.

Figure 2 and Table 1 suggest that DFTB captures the features of the top of the valence band and the bottom of the conduction band with good accuracy, relative to the DFT calculations, and that including SOC in DFTB alters the features of the CB in the same qualitative manner as in DFT. The virtue of using different confinement parameters for DFTB when accounting for SOC is illustrated in the good agreement for the band gap, despite the lack of quasiparticle corrections. The band gap of the tetragonal phase, which is most stable at ambient conditions, is 1.61 eV (1.6 eV with SOC), in excellent agreement with experiment, and its dependence on the variation of atomic structure matches that obtained from scalar relativistic DFT calculations. We note that the addition of SOC in DFTB does not alter significantly this trend. The agreement of the effective masses extracted from the curvatures of the bands within the 5 meV window from the band extrema shows greater relative error, specifically for the conduction band in simulations without SOC. The key issue is the relative flatness of the conduction band, as compared to the valence band and to the more accurate calculations.³⁸ As seen in Figure 2 and Table 1, the error is greatly reduced when SOC is accounted for in DFTB. In this case, the average effective masses over multiple paths in the first Brillouin zone for TET-p structure are 0.22 m_0 (electrons) and 0.24 m_0 (holes), which compare well to results from SOC-GW, 0.19 m_0 and 0.25 m_0 .³⁸ From Table 1 we see also that the effective masses do not vary too much with the structural deformation of MAPbI₃ even if SOC is accounted for.

Finally, we note that, despite the attractive accuracy of DFTB calculations with SOC in terms of band structures, including SOC in the transport calculations is not yet possible. The challenges are 2-fold: first, there is no complete implementation of DFTB+SOC+NEGF, and second, the computation cost increases substantially due to a 4 times larger Hamiltonian matrix and multiple increase of self-consistent cycle iterations, due to the need for angular-momentum-resolved (or orbital-resolved) DFTB. Avoiding that, the transport study excludes SOC, delivering a semiquantitative insight.

3. Quantum Transport. To study the response of the systems to external applied bias, we calculate the steady-state current based on the Keldysh NEGF approach:⁵¹

$$I_\alpha = \frac{2e}{\hbar} \int \frac{dE}{2\pi} \text{Tr}[\Sigma_\alpha^<(E)G^>(E) - \Sigma_\alpha^>(E)G^<(E)] \quad (4)$$

where $G^{\langle \rangle}(E)$ are lesser and greater Green's functions, providing information on the energy states and population statistics for electrons and holes, respectively. $\Sigma_\alpha^{\langle \rangle}(E)$ are the self-energies for the electrode α :

$$\Sigma_\alpha^<(E) = if_\alpha(E)\Gamma_\alpha(E)$$

$$\Sigma_\alpha^>(E) = -i\{1 - f_\alpha(E)\}\Gamma_\alpha(E) \quad (5)$$

where f_α is the electron occupations of electrode α and Γ_α describes the broadening of energy levels due to coupling to electrode α . Thus, the first and second terms on RHS of eq 4 represent, respectively, the incoming and outgoing rate of electrons due to electrode α . Assuming thermal equilibrium of the electrodes, eq 4 reduces to the Landauer–Büttiker formula. For the full details of NEGF, we refer the interested readers to ref 52.

To evaluate radiative recombination rate of charge carriers, we take into account the interactions with photons in the vacuum environment:⁵³

$$R = \int d\omega F(\omega) = \frac{2}{\hbar} \int d\omega \int \frac{dE}{2\pi} \text{Tr}[\Sigma_{\text{ep}}^<(E, \omega)G^>(E)] \quad (6)$$

where R is the carrier recombination rate. $F(\omega)$ is the emission flux for frequency ω . $\Sigma_{\text{ep}}^<(E, \omega)$ is the electron-photon self-energy, which can be expressed as

$$\Sigma_{\text{ep}}^<(E, \omega) = MG^<(E + \hbar\omega)M \quad (7)$$

and M is the electron–photon coupling matrix.^{53,54} Thus, the terms in square bracket on RHS of eq 6 correspond to the transition of an electron from the energy level $E + \hbar\omega$ to E , emitting a photon with energy $\hbar\omega$, and the integrations take into account all energy levels and possible transitions. The method has been recently applied to study electroluminescence of nanoscale light-emitting diodes.⁵³

RESULTS AND DISCUSSION

We first calculate the band structures for the $1 \times 1 \times 4$ supercells with and without ferroelectric domain walls as shown in Figure 3a and b, respectively. Both structures exhibit a direct band gap at Γ point, and the band gap of perovskite with charged domain walls is smaller than that of single domain perovskite. This is consistent with first-principles studies³³ and is a further demonstration of the applicability of DFTB in the field of organometallic halide perovskites. Examination of partial density of states (DOS) shows that, for both structures, states near band gap are mainly contributed from orbitals of Pb and I atoms, while orbitals of methylammonium are away from the band gap. This suggests that the reduction of band gap is mainly caused by the electric potential difference across the domain, which shifts the valence band maximum (VBM) and conduction band minimum (CBM).⁴⁸ Notably the change of the band gap is more pronounced when SOC effects are considered in the calculation, and changes from 0.2 to 0.7 eV reduction. We observe also a concomitant change in the

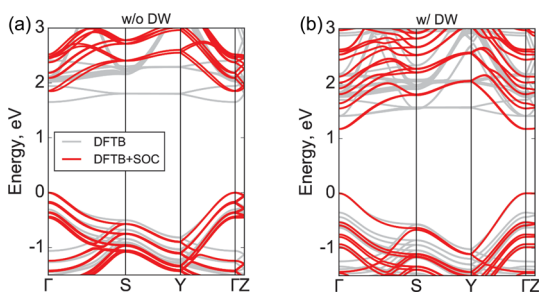


Figure 3. DFTB-calculated band structures for MAPbI₃ perovskites (a) with single domain and (b) with domain structures. The valence band maximum has been shifted to zero. Comparison is made between calculations without SOC (gray lines) and with SOC effects (red lines), showing a much stronger reduction of the band gap for the two-domain structure in the latter case. Notably, both conduction band and valence band seem to be affected by SOC in the two-domain structure, unlike the cases of single domain.

effective masses being more than 10% lower in the two-domain structure. Taking the values along Γ -X from the SOC calculation as representative, the effective electron mass changes from 0.27 to 0.24 [m_0] and the hole mass changes from 0.24 to 0.2 [m_0], in the two-domain structure. The same trend is observed in the valence band from simulations excluding SOC.

The presence of charged domain walls is expected to influence significantly the transport properties of MAPbI₃ perovskites due to the band gap reduction. The current–voltage characteristics of perovskites on both linear and log scale for systems in different ferroelectric states are presented in Figure 4a. Clearly, an enhancement of electronic transport is observed for systems with the presence of charged domain walls. Because of the reduction of band gap, the current onset appears at a lower voltage bias as compared to the single domain structure. For applied voltage up to 2 V, the current in system with domain walls is about 2–3 orders of magnitude larger than that in the single domain system. Further support to our results of enhanced conductance is provided by comparing the difference between the corresponding equilibrium transmission coefficients. Again, comparison is drawn between systems in different ferroelectric states. The transmission spectrum shown in Figure 4b exhibits two features. First, with the presence of charged domain walls, a transport channel

appears at lower energies above the Fermi level. This is also reflected in their band structures where CBM is shifted downward due to the electrostatic potential at ferroelectric domain walls. More interestingly, transmission values are substantially higher at the CBM in the domain wall structure as magnified in the inset of Figure 4b. The results show that domain walls in perovskites have a higher conductance as compared to the bulk materials. The increased conductivity has been previously attributed to charge carrier accumulation at the domain walls.⁵⁵ From the perspective of quantum transport, the enhanced conduction corresponds to an increased DOS and stronger couplings to the electrodes at the domain walls.

Because of the ferroelectric domain walls, previous studies had suggested that electrons and holes in perovskites can diffuse separately along distinct pathways toward the electrodes, avoiding carriers of opposite charge. To spatially reveal the features of transport pathways' segregation within the devices, we calculate the local DOS at VBM and CBM, which are shown in Figure 5 for MAPbI₃ in both ferroelectric states. The logarithm of the DOS projected on the xz -plane in the middle of the supercell is shown. It is notable that for perovskites containing domain walls, energy states at VBM and CBM are located along the transport direction at the tail-to-tail and head-to-head domain walls, respectively. Thus, the channels for electrons and holes are spatially separated. This is in contrast to the system with single domain where energy states at VBM and CBM are delocalized over the entire system, as shown in Figure 5c and d. From the local DOS plot, it is expected that with the presence of domain structures, the probability of electron–hole recombination will be suppressed due to the separate channels for electrons and holes.

To further verify the role of ferroelectric domain walls, we evaluate the electron–hole recombination rate for the studied systems using eq 6. In realistic photovoltaic devices, electrons are photoexcited to the conduction band, leaving holes in the valence band. Because of the internal electric field caused by different electrode work functions, electrons and holes are driven in opposite directions. Here, we investigate the radiative recombinations of band-edge carriers. The device operating conditions are modeled by directly injecting electrons and holes into the conduction band and valence band edges, respectively. This is done by adding a Lorentz distribution of carriers to the electron (f_α) and hole ($1 - f_\alpha$) occupations at the corresponding energies in eq 5. By doing that, hot carriers

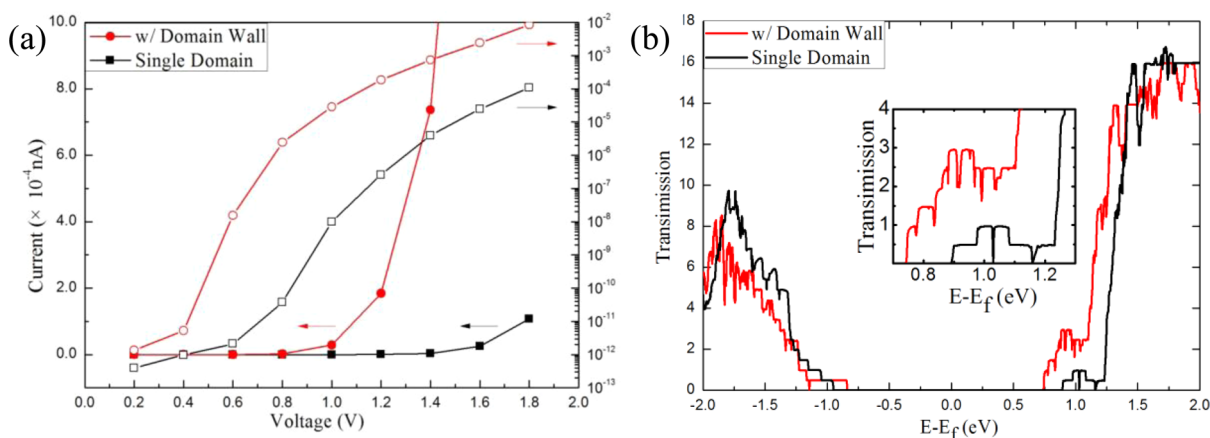


Figure 4. (a) Current–voltage characteristics and (b) equilibrium transmission coefficients as a function of energy for MAPbI₃ perovskite with and without domain walls. Fermi energy is shifted to $E = 0$.

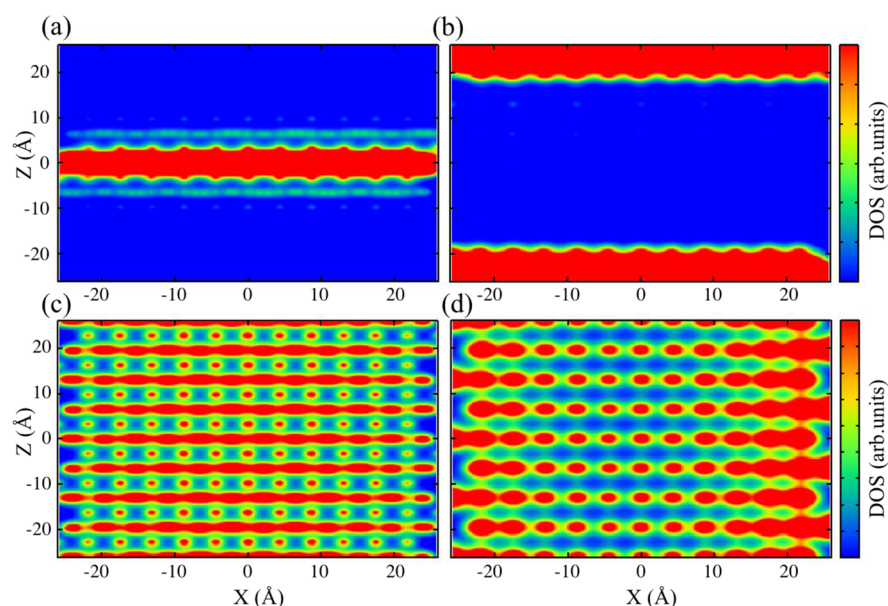


Figure 5. Local DOS at VBM (left) and CBM (right) in xz plane for MAPbI₃ perovskite: (a and b) with domain structures; and (c and d) single domain.

are assumed to relax to band edges before radiative recombinations occur. The emission frequency range in eq 5 is taken from 1.55 to 1.90 eV, which covers the band gaps for both systems of different ferroelectric states. The recombination rates for the studied systems are summarized in Table 2. As

Table 2. Comparison of Radiative Recombination Rates between MAPbI₃ of Different Ferroelectric States and Channel Lengths

device thickness (nm)	recombination rate (s ⁻¹)	
	single domain	with domain walls
5.24	1.21×10^{-8}	8.20×10^{-12}
10.49	1.34×10^{-8}	5.71×10^{-11}

expected, due to the distinct transport channels for electrons and holes, charge carrier recombination is substantially suppressed in perovskites with domain structures. The recombination rate is about 3–4 orders of magnitude lower than that in perovskite of single domain. We further investigate the recombination of charge carriers for devices of different thicknesses. Devices with larger thickness are constructed by extending the central region along the transport direction. In general, a higher recombination rate is observed for larger device thickness due to the increase number of carriers within the devices. A recent experiment reports the observation of long-lived energetic carriers in organometallic halide perovskites, which is correlated with reorientation motions of molecular dipoles.⁵⁶ The current study suggests that ferroelectric domain walls may provide one possible mechanism for the protection of charge carriers in perovskites from scatterings. However, further studies are needed to understand the dynamic screening mechanism.

CONCLUSIONS

In summary, the electronic transport properties due to ferroelectric domain walls in organometallic halide perovskites are studied via DFTB simulations in combination with NEGF method. We parametrized MAPbI₃ perovskite materials for the

DFTB method, and commendable agreement is achieved in comparison to quasiparticle GW calculations. Enhancement of electronic transport is observed for systems with domain structures due to the reduced band gap. In addition, our results show that ferroelectric domains in MAPbI₃ lead to segregation of transport pathways for electrons and holes, and thus carrier recombination is substantially suppressed. Our findings indicate that ferroelectric domains have an important role in the outstanding performance of organometallic halide perovskites for photovoltaic applications. The results presented in this Article advance our understanding of the interplay of structural properties and photovoltaic performance in the material, which is useful for discerning and engineering the performance of the energy conversion mechanism.

AUTHOR INFORMATION

Corresponding Author

*Phone: 86-10-56981819. E-mail: yamcy@csrc.ac.cn.

ORCID

Limin Liu: 0000-0003-3925-5310

Xiao Zheng: 0000-0002-9804-1833

ChiYung Yam: 0000-0002-3860-2934

Notes

The authors declare no competing financial interest.

ACKNOWLEDGMENTS

The financial support from the National Natural Science Foundation of China (Grant nos. 21322306 (C.Y.Y.), 21673017 (C.Y.Y.), and U1530401 (C.Y.Y.)), the National Basic Research Program of China (Grant no. 2014CB921402 (C.Y.Y.)), and the University Grant Council (Grant no. AoE/P-04/08 (G.H.C., C.Y.Y.)) is gratefully acknowledged. Computational support has been provided by the Special Program for Applied Research on Super Computation of the NSFC-Guangdong Joint Fund and Beijing Computational Science Research Center (CSRC).

REFERENCES

- (1) Kojima, A.; Teshima, K.; Shirai, Y.; Miyasaka, T. Organometal Halide Perovskites as Visible-light Sensitizers for Photovoltaic Cells. *J. Am. Chem. Soc.* **2009**, *131*, 6050–6051.
- (2) Yang, W. S.; Noh, J. H.; Jeon, N. J.; Kim, Y. C.; Ryu, S.; Seo, J.; Seok, S. I. High-performance Photovoltaic Perovskite Layers Fabricated through Intramolecular Exchange. *Science* **2015**, *348*, 1234–1237.
- (3) Zhao, Y.; Zhu, K. Organic-inorganic Hybrid Lead Halide Perovskites for Optoelectronic and Electronic Applications. *Chem. Soc. Rev.* **2016**, *45*, 655–689.
- (4) McGehee, M. D. Perovskite Solar Cells: Continuing to Soar. *Nat. Mater.* **2014**, *13*, 845–846.
- (5) Hao, F.; Stoumpos, C. C.; Cao, D. H.; Chang, R. P. H.; Kanatzidis, M. G. Lead-free Solid-state Organic-inorganic Halide Perovskite Solar Cells. *Nat. Photonics* **2014**, *8*, 489–494.
- (6) Ogomi, Y.; Morita, A.; Tsukamoto, S.; Saitho, T.; Fujikawa, N.; Shen, Q.; Toyoda, T.; Yoshino, K.; Pandey, S. S.; Ma, T.; et al. $\text{CH}_3\text{NH}_3\text{SnPb}_{(1-x)}\text{I}_3$ Perovskite Solar Cells Covering up to 1060 nm. *J. Phys. Chem. Lett.* **2014**, *5*, 1004–1011.
- (7) Blancon, J.-C.; Nie, W.; Neukirch, A. J.; Gupta, G.; Tretiak, S.; Cognet, L.; Mohite, A. D.; Crochet, J. J. The Effects of Electronic Impurities and Electron–Hole Recombination Dynamics on Large-Grain Organic–Inorganic Perovskite Photovoltaic Efficiencies. *Adv. Funct. Mater.* **2016**, *26*, 4283–4292.
- (8) Stranks, S. D.; Eperon, G. E.; Grancini, G.; Menelaou, C.; Alcocer, M. J. P.; Leijtens, T.; Herz, L. M.; Petrozza, A.; Snaith, H. J. Electron-Hole Diffusion Lengths Exceeding 1 Micrometer in an Organometal Trihalide Perovskite Absorber. *Science* **2013**, *342*, 341–344.
- (9) Tian, W.; Cui, R.; Leng, J.; Liu, J.; Li, Y.; Zhao, C.; Zhang, J.; Deng, W.; Lian, T.; Jin, S. Limiting Perovskite Solar Cell Performance by Heterogeneous Carrier Extraction. *Angew. Chem.* **2016**, *128*, 13261–13265.
- (10) Chen, B.; Yang, M.; Priya, S.; Zhu, K. Origin of J–V Hysteresis in Perovskite Solar Cells. *J. Phys. Chem. Lett.* **2016**, *7*, 905–917.
- (11) Juarez-Perez, E. J.; Sanchez, R. S.; Badia, L.; Garcia-Belmonte, G.; Kang, Y. S.; Mora-Sero, I.; Bisquert, J. Photoinduced Giant Dielectric Constant in Lead Halide Perovskite Solar Cells. *J. Phys. Chem. Lett.* **2014**, *5*, 2390–2394.
- (12) Xiao, Z.; Yuan, Y.; Shao, Y.; Wang, Q.; Dong, Q.; Bi, C.; Sharma, P.; Gruverman, A.; Huang, J. Giant Switchable Photovoltaic Effect in Organometal Trihalide Perovskite Devices. *Nat. Mater.* **2015**, *14*, 193–198.
- (13) Gottesman, R.; Gouda, L.; Kalanoor, B. S.; Haltzi, E.; Tirosh, S.; Rosh-Hodesh, E.; Tischler, Y.; Zaban, A.; Quarti, C.; Mosconi, E.; et al. Photoinduced Reversible Structural Transformations in Free-standing $\text{CH}_3\text{NH}_3\text{PbI}_3$ Perovskite Films. *J. Phys. Chem. Lett.* **2015**, *6*, 2332–2338.
- (14) Hoke, E. T.; Slotcavage, D. J.; Dohner, E. R.; Bowring, A. R.; Karunadasa, H. I.; McGehee, M. D. Reversible Photo-induced Trap Formation in Mixed-halide Hybrid Perovskites for Photovoltaics. *Chem. Sci.* **2015**, *6*, 613–617.
- (15) Stoumpos, C. C.; Malliakas, C. D.; Kanatzidis, M. G. Semiconducting Tin and Lead Iodide Perovskites with Organic Cations: Phase Transitions, High Mobilities, and Near-Infrared Photoluminescent Properties. *Inorg. Chem.* **2013**, *52*, 9019–9038.
- (16) Kutes, Y.; Ye, L.; Zhou, Y.; Pang, S.; Huey, B. D.; Padture, N. P. Direct Observation of Ferroelectric Domains in Solution-processed $\text{CH}_3\text{NH}_3\text{PbI}_3$ Perovskite Thin Films. *J. Phys. Chem. Lett.* **2014**, *5*, 3335–3339.
- (17) Kim, Y.-J.; Dang, T.-V.; Choi, H.-J.; Park, B.-J.; Eom, J.-H.; Song, H.-A.; Seol, D.; Kim, Y.; Shin, S.-H.; Nah, J.; et al. Piezoelectric Properties of $\text{CH}_3\text{NH}_3\text{PbI}_3$ Perovskite Thin Films and Their Applications in Piezoelectric Generators. *J. Mater. Chem. A* **2016**, *4*, 756–763.
- (18) Coll, M.; Gomez, A.; Mas-Marza, E.; Almora, O.; Garcia-Belmonte, G.; Campoy-Quiles, M.; Bisquert, J. Polarization Switching and Light-enhanced Piezoelectricity in Lead Halide Perovskites. *J. Phys. Chem. Lett.* **2015**, *6*, 1408–1413.
- (19) Solmaz, A.; Huijben, M.; Koster, G.; Egoavil, R.; Gauquelin, N.; Van Tendeloo, G.; Verbeeck, J.; Noheda, B.; Rijnders, G. Domain Selectivity in BiFeO_3 Thin Films by Modified Substrate Termination. *Adv. Funct. Mater.* **2016**, *26*, 2882–2889.
- (20) Yan, F.; Zhu, T. J.; Lai, M. O.; Lu, L. Effect of Bottom Electrodes on Nanoscale Switching Characteristics and Piezoelectric Response in Polycrystalline BiFeO_3 Thin Films. *J. Appl. Phys.* **2011**, *110*, 084102.
- (21) Rakita, Y.; Bar-Elli, O.; Meirzadeh, E.; Kaslasi, H.; Peleg, Y.; Hodes, G.; Lubo-mirsky, I.; Oron, D.; Ehre, D.; Cahen, D. Tetragonal $\text{CH}_3\text{NH}_3\text{PbI}_3$ Is Ferroelectric. *ArXiv e-prints* **2017**, arXiv:1702.05267.
- (22) Frost, J. M.; Butler, K. T.; Brivio, F.; Hendon, C. H.; van Schilfgaarde, M.; Walsh, A. Atomistic Origins of High-performance in Hybrid Halide Perovskite Solar Cells. *Nano Lett.* **2014**, *14*, 2584–2590.
- (23) Zheng, F.; Takenaka, H.; Wang, F.; Koocher, N. Z.; Rappe, A. M. First-principles Calculation of the Bulk Photovoltaic Effect in $\text{CH}_3\text{NH}_3\text{PbI}_3$ and $\text{CH}_3\text{NH}_3\text{PbI}_{3-x}\text{Cl}_x$. *J. Phys. Chem. Lett.* **2015**, *6*, 31–37.
- (24) Quarti, C.; Mosconi, E.; De Angelis, F. Interplay of Orientational Order and Electronic Structure in Methylammonium Lead Iodide: Implications for Solar Cell Operation. *Chem. Mater.* **2014**, *26*, 6557–6569.
- (25) Stroppa, A.; Quarti, C.; De Angelis, F.; Picozzi, S. Ferroelectric Polarization of $\text{CH}_3\text{NH}_3\text{PbI}_3$: A Detailed Study Based on Density Functional Theory and Symmetry Mode Analysis. *J. Phys. Chem. Lett.* **2015**, *6*, 2223–2231.
- (26) Fan, Z.; Xiao, J.; Sun, K.; Chen, L.; Hu, Y.; Ouyang, J.; Ong, K. P.; Zeng, K.; Wang, J. Ferroelectricity of $\text{CH}_3\text{NH}_3\text{PbI}_3$ Perovskite. *J. Phys. Chem. Lett.* **2015**, *6*, 1155–1161.
- (27) Goehry, C.; Nemnes, G. A.; Manolescu, A. Collective Behavior of Molecular Dipoles in $\text{CH}_3\text{NH}_3\text{PbI}_3$. *J. Phys. Chem. C* **2015**, *119*, 19674–19680.
- (28) Grinberg, I.; West, D. V.; Torres, M.; Gou, G.; Stein, D. M.; Wu, L.; Chen, G.; Gallo, E. M.; Akbashev, A. R.; Davies, P. K.; et al. Perovskite Oxides for Visible-light-absorbing Ferroelectric and Photovoltaic Materials. *Nature* **2013**, *503*, 509–512.
- (29) Yang, S. Y.; Seidel, J.; Byrnes, S. J.; Shafer, P.; Yang, C. H.; Rossell, M. D.; Yu, P.; Chu, Y. H.; Scott, J. F.; Ager, J. W.; et al. Above-bandgap Voltages from Ferroelectric Photovoltaic Devices. *Nat. Nanotechnol.* **2010**, *5*, 143–147.
- (30) Shockley, W.; Queisser, H. J. Detailed Balance Limit of Efficiency of P-N Junction Solar Cells. *J. Appl. Phys.* **1961**, *32*, 510–519.
- (31) Etienne, T.; Mosconi, E.; De Angelis, F. Dynamical Origin of the Rashba Effect in Organohalide Lead Perovskites: A Key to Suppressed Carrier Recombination in Perovskite Solar Cells? *J. Phys. Chem. Lett.* **2016**, *7*, 1638–1645.
- (32) Pecchia, A.; Gentilini, D.; Rossi, D.; Auf der Maur, M.; Di Carlo, A. Role of Ferroelectric Nanodomains in the Transport Properties of Perovskite Solar Cells. *Nano Lett.* **2016**, *16*, 988–992.
- (33) Liu, S.; Zheng, F.; Koocher, N. Z.; Takenaka, H.; Wang, F.; Rappe, A. M. Ferroelectric Domain Wall Induced Band Gap Reduction and Charge Separation in Organometal Halide Perovskites. *J. Phys. Chem. Lett.* **2015**, *6*, 693–699.
- (34) Berdiyrov, G. R.; El-Mellouhi, F.; Madjet, M. E.; Alharbi, F. H.; Rashkeev, S. N. Electronic Transport in Organometallic Perovskite $\text{CH}_3\text{NH}_3\text{PbI}_3$: The Role of Organic Cation Orientations. *Appl. Phys. Lett.* **2016**, *108*, 053901.
- (35) Ma, J.; Wang, L.-W. Nanoscale Charge Localization Induced by Random Orientations of Organic Molecules in Hybrid Perovskite $\text{CH}_3\text{NH}_3\text{PbI}_3$. *Nano Lett.* **2015**, *15*, 248–253.
- (36) Zhang, X.; Zhang, M.; Lu, G. Charge Stripe Formation in Molecular Ferroelectric Organohalide Perovskites for Efficient Charge Separation. *J. Phys. Chem. C* **2016**, *120*, 23969–23975.

(37) Pecchia, A.; Penazzi, G.; Salvucci, L.; Carlo, A. D. Non-equilibrium Green's Functions in Density Functional Tight Binding: Method and Applications. *New J. Phys.* **2008**, *10*, 065022.

(38) Umari, P.; Mosconi, E.; De Angelis, F. Relativistic GW Calculations on $\text{CH}_3\text{NH}_3\text{PbI}_3$ and $\text{CH}_3\text{NH}_3\text{SnI}_3$ Perovskites for Solar Cell Applications. *Sci. Rep.* **2014**, *4*, 4467.

(39) Kresse, G.; Furthmüller, J. Efficient Iterative Schemes for *ab initio* Total-energy Calculations Using a Plane-wave Basis Set. *Phys. Rev. B: Condens. Matter Mater. Phys.* **1996**, *54*, 11169–11186.

(40) Perdew, J. P.; Burke, K.; Ernzerhof, M. Generalized Gradient Approximation Made Simple. *Phys. Rev. Lett.* **1996**, *77*, 3865–3868.

(41) Dion, M.; Rydberg, H.; Schröder, E.; Langreth, D. C.; Lundqvist, B. I. Van der Waals Density Functional for General Geometries. *Phys. Rev. Lett.* **2004**, *92*, 246401.

(42) Kresse, G.; Joubert, D. From Ultrasoft Pseudopotentials to the Projector Augmented-wave Method. *Phys. Rev. B: Condens. Matter Mater. Phys.* **1999**, *59*, 1758–1775.

(43) Elstner, M.; Porezag, D.; Jungnickel, G.; Elsner, J.; Haugk, M.; Frauenheim, T.; Suhai, S.; Seifert, G. Self-consistent-charge Density-functional Tight-binding Method for Simulations of Complex Materials Properties. *Phys. Rev. B: Condens. Matter Mater. Phys.* **1998**, *58*, 7260–7268.

(44) Kubař, T.; Bodrog, Z.; Gaus, M.; Köhler, C.; Aradi, B.; Frauenheim, T.; Elstner, M. Parametrization of the SCC-DFTB Method for Halogens. *J. Chem. Theory Comput.* **2013**, *9*, 2939–2949.

(45) Wahiduzzaman, M.; Oliveira, A. F.; Philipsen, P.; Zhechkov, L.; van Lenthe, E.; Witek, H. A.; Heine, T. DFTB Parameters for the Periodic Table: Part 1, Electronic Structure. *J. Chem. Theory Comput.* **2013**, *9*, 4006–4017.

(46) Zheng, F.; Tan, L. Z.; Liu, S.; Rappe, A. M. Rashba Spin–Orbit Coupling Enhanced Carrier Lifetime in $\text{CH}_3\text{NH}_3\text{PbI}_3$. *Nano Lett.* **2015**, *15*, 7794–7800.

(47) Aradi, B.; Hourahine, B.; Frauenheim, T. DFTB+, a Sparse Matrix-Based Implementation of the DFTB Method. *J. Phys. Chem. A* **2007**, *111*, 5678–5684.

(48) Sluka, T.; Tagantsev, A. K.; Damjanovic, D.; Gureev, M.; Setter, N. Enhanced Electromechanical Response of Ferroelectrics due to Charged Domain Walls. *Nat. Commun.* **2012**, *3*, 748.

(49) Gmitra, M.; Kunschuh, S.; Ertler, C.; Ambrosch-Draxl, C.; Fabian, J. Band-structure Topologies of Graphene: Spin-orbit Coupling Effects from First Principles. *Phys. Rev. B: Condens. Matter Mater. Phys.* **2009**, *80*, 235431.

(50) Geng, W.; Zhang, L.; Zhang, Y. N.; Lau, W. M.; Liu, L. M. First-Principles Study of Lead Iodide Perovskite Tetragonal and Orthorhombic Phases for Photovoltaics. *J. Phys. Chem. C* **2014**, *118*, 19565–19571.

(51) Meir, Y.; Wingreen, N. S. Landauer Formula for the Current through an Interacting Electron Region. *Phys. Rev. Lett.* **1992**, *68*, 2512–2515.

(52) Datta, S. *Electronic Transport in Mesoscopic Systems*; Cambridge University Press: Cambridge, UK, 1997.

(53) Wang, R.; Zhang, Y.; Bi, F.; Frauenheim, T.; Chen, G.; Yam, C. Quantum Mechanical Modeling the Emission Pattern and Polarization of Nanoscale Light Emitting Diodes. *Nanoscale* **2016**, *8*, 13168–13173.

(54) Zhang, Y.; Meng, L.; Yam, C.; Chen, G. Quantum-Mechanical Prediction of Nanoscale Photovoltaics. *J. Phys. Chem. Lett.* **2014**, *5*, 1272–1277.

(55) Rashkeev, S. N.; El-Mellouhi, F.; Kais, S.; Alharbi, F. H. Domain Walls Conductivity in Hybrid Organometallic Perovskites and Their Essential Role in $\text{CH}_3\text{NH}_3\text{PbI}_3$ Solar Cell High Performance. *Sci. Rep.* **2015**, *5*, 11467.

(56) Zhu, H.; Miyata, K.; Fu, Y.; Wang, J.; Joshi, P. P.; Niesner, D.; Williams, K. W.; Jin, S.; Zhu, X. Y. Screening in Crystalline Liquids Protects Energetic Carriers in Hybrid Perovskites. *Science* **2016**, *353*, 1409.